

# Strain-Engineered Oxygen Vacancies in $\text{CaMnO}_3$ Thin Films

Ravini U. Chandrasena,<sup>†,‡,§</sup> Weibing Yang,<sup>†,‡</sup> Qingyu Lei,<sup>†,‡</sup> Mario U. Delgado-Jaime,<sup>§</sup> Kanishka D. Wijesekara,<sup>†,‡</sup> Maryam Golalikhani,<sup>†,‡</sup> Bruce A. Davidson,<sup>†</sup> Elke Arenholz,<sup>||</sup> Keisuke Kobayashi,<sup>⊥</sup> Masaaki Kobata,<sup>⊥</sup> Frank M. F. de Groot,<sup>§</sup> Ulrich Aschauer,<sup>#,∇</sup> Nicola A. Spaldin,<sup>#</sup> Xiaoxing Xi,<sup>†,‡</sup> and Alexander X. Gray<sup>\*,†,‡</sup>

<sup>†</sup>Department of Physics, Temple University, 1925 North 12th Street, Philadelphia, Pennsylvania 19122, United States

<sup>‡</sup>Temple Materials Institute, Temple University, 1925 North 12th Street, Philadelphia, Pennsylvania 19122, United States

<sup>§</sup>Inorganic Chemistry & Catalysis, Debye Institute for Nanomaterials Science, Utrecht University, Universiteitsweg 99, Utrecht 3584 CG, The Netherlands

<sup>||</sup>Advanced Light Source, Lawrence Berkeley National Laboratory, One Cyclotron Road, Berkeley, California 94720, United States

<sup>⊥</sup>Materials Sciences Research Center, Japan Atomic Energy Agency, 1-1-1 Kouto, Sayo-cho, Hyogo 679-5148, Japan

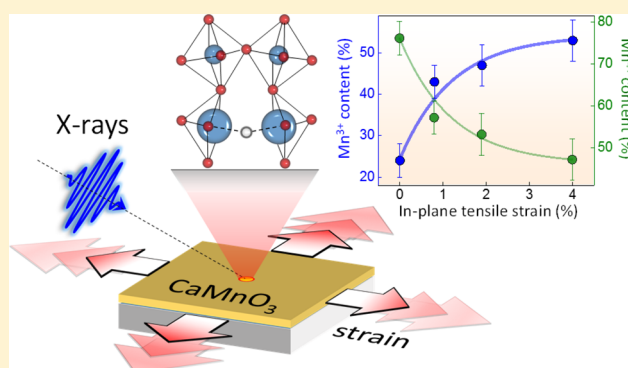
<sup>#</sup>Materials Theory, ETH Zurich, Wolfgang-Pauli-Strasse 27, CH-8093 Zürich, Switzerland

<sup>∇</sup>Department of Chemistry and Biochemistry, University of Bern, Freiestrasse 3, CH-3012 Bern, Switzerland

## Supporting Information

**ABSTRACT:** We demonstrate a novel pathway to control and stabilize oxygen vacancies in complex transition-metal oxide thin films. Using atomic layer-by-layer pulsed laser deposition (PLD) from two separate targets, we synthesize high-quality single-crystalline  $\text{CaMnO}_3$  films with systematically varying oxygen vacancy defect formation energies as controlled by coherent tensile strain. The systematic increase of the oxygen vacancy content in  $\text{CaMnO}_3$  as a function of applied in-plane strain is observed and confirmed experimentally using high-resolution soft X-ray absorption spectroscopy (XAS) in conjunction with bulk-sensitive hard X-ray photoemission spectroscopy (HAXPES). The relevant defect states in the densities of states are identified and the vacancy content in the films quantified using the combination of first-principles theory and core–hole multiplet calculations with holistic fitting. Our findings open up a promising avenue for designing and controlling new ionically active properties and functionalities of complex transition-metal oxides via strain-induced oxygen-vacancy formation and ordering.

**KEYWORDS:** Strongly correlated oxides, strain engineering, oxygen vacancies, X-ray spectroscopy



Dynamic control of ionic defects in transition-metal oxides and their interfaces is considered to be an exciting new avenue toward creating materials with novel electronic, magnetic, and structural properties.<sup>1,2</sup> Such an approach for materials design, strongly reminiscent of the principles that enable modern semiconductor technology, has tremendous potential due to the fact that very small changes in the concentrations of defects such as oxygen vacancies can lead to dramatic changes in the materials' properties and function, such as conductivity<sup>3</sup> and magnetism.<sup>4</sup> Thus, our ability to tailor and fine-tune the densities and concentration profiles of such functional defects largely determines the full range of novel phenomena and functionalities accessible in such systems.

Coherent epitaxial strain has been widely utilized as a tuning knob to control key functional properties in transition-metal oxides. Recent examples of such strain-functionality coupling

include the control of metal-to-insulator transition temperature in  $\text{VO}_2$ <sup>5</sup> and the insulator-to-superconductor transition temperature in  $\text{La}_{1.9}\text{Sr}_{0.1}\text{CuO}_4$ .<sup>6</sup> Going beyond the ability to effectively manipulate already existing physical properties of a given material, strain has also been shown to invoke entirely new exotic ground states such as ferroelectricity in  $\text{SrTiO}_3$  and increased ferroelectric polarization in  $\text{BaTiO}_3$ , consistent with theoretical predictions.<sup>7–9</sup>

The antiferromagnetic Mott insulator  $\text{CaMnO}_3$  is a well-established example of a complex transition-metal oxide in which electronic and magnetic properties can be manipulated via strain, heteroengineering, and external stimuli.<sup>10–14</sup> A recent

**Received:** September 23, 2016

**Revised:** January 10, 2017

**Published:** January 19, 2017

theoretical study suggests that, in addition to directly affecting internal bond lengths and oxygen octahedral rotations, coherent epitaxial strain can facilitate spontaneous formation of oxygen vacancies and even influence defect-site preference leading to vacancy ordering in  $\text{CaMnO}_3$  and similar materials.<sup>15,16</sup> This prediction opens the door for exploring and controlling new properties and functionalities stemming from ionic activity. Thus, a clear understanding of the energetics and strain-control of such defects is crucial for achieving technical feasibility and efficient performance of future electronic devices relying on these properties.

Here we use a combination of atomic layer-by-layer pulsed laser deposition (PLD) from two separate targets, bulk-sensitive X-ray spectroscopies (XAS and HAXPES), and a combination of theoretical methods to show a direct relationship between applied coherent epitaxial strain and oxygen vacancy concentration in ultrathin single-crystalline  $\text{CaMnO}_3$  films. Spectroscopic fingerprints of the defect-induced electronic states are identified and analyzed. It is furthermore revealed that, due to their high mobility,<sup>17,18</sup> the vacancies partially diffuse out of the film when exposed to ambient atmosphere, thus necessitating an in situ-grown capping layer to preserve the original strain-induced oxygen-vacancy content. This underlines the importance of bulk-sensitive X-ray techniques, capable of probing buried layers and interfaces, for the understanding of the electronic properties of strain-engineered thin films.

Two identical sets of ultrathin (10 unit cells) single-crystalline  $\text{CaMnO}_3$  films were synthesized using atomic layer-by-layer PLD<sup>19</sup> on three different single-crystalline substrates inducing coherent in-plane tensile strain varying from +0.8% to +4% (see Supporting Information for details). Coherent epitaxy at such high strain levels is made possible by atomic layer-by-layer synthesis via alternating ablation of two separate constituent oxide targets ( $\text{MnO}_2$  and  $\text{CaO}$ ).<sup>19</sup> A thicker (80 unit cells) bulk-like  $\text{CaMnO}_3$  film was grown on a  $\text{SrTiO}_3$  substrate as a fully relaxed (0% strain) reference sample. To investigate the effect of ambient atmospheric exposure on the oxygen-vacancy content, one complete set of films was capped with a 3 nm-thick Pt capping layer in situ, and the other identical set synthesized during the same run was left exposed. Quality, crystallinity, and thickness of the films was verified using X-ray diffraction (XRD) and reflection high-energy electron diffraction (RHEED) measurements (see Figure S1 and accompanying discussion in the Supporting Information). In addition, an exhaustive characterization of such coherently strained  $\text{CaMnO}_3$  films via XRD, X-ray reflectivity, and atomic force microscopy was carried out by us in a prior study,<sup>20</sup> confirming crystallinity, tensile strain values, phase purity, and coherence.

Soft X-ray XAS measurements at the Mn  $L_{2,3}$  and O  $K$  absorption thresholds were carried out at the elliptically polarized undulator beamline 4.0.2 of the Advanced Light Source using the Vector Magnet endstation.<sup>21</sup> The average probing depth in the total electron yield XAS detection mode was estimated to be approximately 5 nm, providing optimal bulk-sensitivity to probe the buried  $\text{CaMnO}_3$  layer underneath the 3 nm-thick Pt cap. Measurements were carried out at several locations on the sample, to exclude the possibility of X-ray sample damage.

Complementary core-level HAXPES measurements of the Mn 3s multiplet-split spectra were carried out using a focused monochromated Cr  $K\alpha$  X-ray source integrated with a VG

Scienta R4000 hemispherical analyzer<sup>22</sup> equipped with an additional wide acceptance objective lens. At the Cr  $K\alpha$  excitation energy of 5.4 keV, the inelastic mean-free paths (IMFP) of the photoemitted Mn 3s electrons in  $\text{CaMnO}_3$  and Pt are estimated to be 8.0 and 4.4 nm, respectively.<sup>23</sup> Therefore, HAXPES has an advantage over traditional XPS of being able to probe these electronic states in a buried layer and through the 3 nm-thick Pt cap.

Observed strain-dependent changes in the electronic structure of buried  $\text{CaMnO}_3$  films strongly suggest systematic variation in the Mn valence state due to oxygen vacancy formation with increased tensile strain,<sup>15</sup> as described in the following paragraphs.

We first discuss the changes in the Mn valence state and conduction-band orbital energetics as a function of in-plane strain. The excess charge associated with a neutral oxygen vacancy in  $\text{CaMnO}_3$  is accommodated in the lattice via the reduction of two  $\text{Mn}^{4+}$  to  $\text{Mn}^{3+}$  on sites adjacent to the vacancy.<sup>24</sup> Tensile strain thus lowers the oxygen vacancy formation energy since the expanded lattice facilitates the increase in ionic radius associated with these reduction reactions.<sup>15</sup>

In Figure 1a, we plot the XAS spectra of the Mn  $L_{2,3}$  edges for the four Pt-capped  $\text{CaMnO}_3$  films exhibiting tensile strain ranging from 0% (fully relaxed film) to 4%, as grown on an  $(\text{LaAlO}_3)_{0.3}(\text{Sr}_2\text{AlTaO}_6)_{0.7}$  (LSAT) substrate. XAS at the  $L_{2,3}$  edges has been used routinely for the analysis of the transition-metal valence states in oxides.<sup>25,26</sup> Spin-orbit coupling splits the transition-metal  $L_{2,3}$  edge into two components,  $L_2$  and  $L_3$ , corresponding to the  $2p_{1/2} \rightarrow 3d$  and  $2p_{3/2} \rightarrow 3d$  transitions, respectively.<sup>25,26</sup> The most striking evidence of the changes in the Mn valence state toward  $\text{Mn}^{3+}$  is observed with the systematic shift of the  $L_2$  and  $L_3$  spectral weights toward lower photon energies<sup>26–29</sup> as a function of increasing strain. The spectral shift is due to changes in the electrostatic energy at the Mn site driven by the decrease in the 3d count, which leads to shifts of both the core level and the final-state wave functions.<sup>27,30</sup> The observed total chemical shift of approximately 0.7 eV is immediately obvious to the eye for the  $L_2$  edge (see Figure 1a) and can be verified for the  $L_3$  edge via appropriate peak fitting, which is necessary due to the more complex structure of the excitonic region of the  $L_3$  edge.

In addition to the above-mentioned chemical shift, increase of the  $\text{Mn}^{3+}$  content with increased tensile strain is evidenced by the systematic increase in spectral weight of the feature at the photon energy of 640.3 eV, shown in the outset of Figure 1a, and identified in prior studies as the signature of the  $\text{Mn}^{3+}$  high-spin valence state.<sup>31,32</sup> Ratios of the spectral weight of the  $\text{Mn}^{3+}$  peak to the total spectral weight of the  $L_3$  edge, obtained via background subtraction and peak-fitting, are plotted in Figure 1b and exhibit monotonic increase as a function of strain. Corresponding systematic changes in the strain-dependent oxygen vacancy formation energies, calculated using density functional theory as in ref 15, are plotted on the left axis and shown by green symbols.

Another indicator of the increase of the  $\text{Mn}^{3+}$  content, the  $L_3/L_2$  intensity ratio that is highly sensitive to the valence state of Mn ions,<sup>33,34</sup> is calculated and plotted in Figure 1b as a function of tensile strain. For the fully relaxed bulk-like  $\text{CaMnO}_3$  film, the ratio is the lowest of the series (close to 2), consistent with the  $d^3$  configuration of the predominant  $\text{Mn}^{4+}$  ion.<sup>33</sup> The ratio grows as a function of increased tensile strain (see Figure 1b), which strongly suggests an increase in the

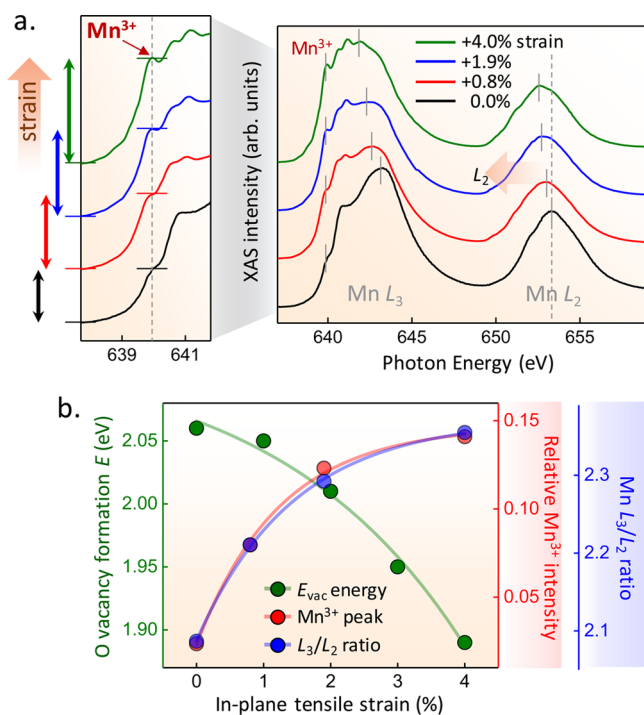


**Figure 1.** (a) Mn  $L_{2,3}$  XAS spectroscopy of the strained ultrathin  $\text{CaMnO}_3$  films. Systematic evolution of the spectroscopic features at the Mn  $L_{2,3}$  edges observed with substrate-induced tensile strain is consistent with the increase in the  $\text{Mn}^{3+}$  ion concentration induced by the oxygen vacancy formation. The key features include the chemical shift of the  $L_2$  and  $L_3$  spectral weights toward lower photon energies,<sup>26,27</sup> increase in the spectral weight of the  $\text{Mn}^{3+}$  high spin valence state feature at approximately 640.3 eV (inset),<sup>31,32</sup> and the growth of the  $L_3/L_2$  ratio.<sup>33,34</sup> (b) Experimental data (right axis) showing the continuous systematic variation of the  $\text{Mn}^{3+}$  feature intensity as normalized to the total  $L_3$  peak area (red markers) and the  $L_3/L_2$  ratio (blue markers) are correlated to the calculated strain-dependent oxygen vacancy formation energy (left axis/green markers). Both the experimental and theoretical values are plotted as functions of in-plane tensile strain.

concentration of  $\text{Mn}^{3+}$  ions with  $d^4$  configuration.<sup>33</sup> Consistent with the  $\text{Mn}^{3+}$  peak intensities, the  $L_3/L_2$  ratios are also correlated to the calculated oxygen vacancy formation energies for the respective strain values.

To determine the  $\text{Mn}^{3+}$  and  $\text{Mn}^{4+}$  ionic content in each sample, we simultaneously and self-consistently fit our experimental data using spectra calculated for the respective Mn species via multiplet simulations.<sup>35,36</sup> In our model, the corresponding reductions of Slater integrals (which account for covalency) and the crystal-field parameters, in combination with Lorentzian and Gaussian broadenings, are all treated as the fit parameters. The edge jumps, modeled as cumulative pseudo-Voigt functions, and background functions are included for each data set. The resultant reference spectra for the  $\text{Mn}^{3+}$  and  $\text{Mn}^{4+}$  species are applied simultaneously to all data sets, with a common energy shift and varying scaling factors to account for the differences in composition between different samples. The fitting is performed using the Blueprint XAS package,<sup>35,36</sup> which enables calculations of multiple fits from multiple reduced-bias starting points, making it possible to evaluate uncertainties in the fit parameters as well as the derived quantities. Figure 2a shows the resultant fits with the two optimized reference spectra calculated for the  $\text{Mn}^{3+}$  and  $\text{Mn}^{4+}$

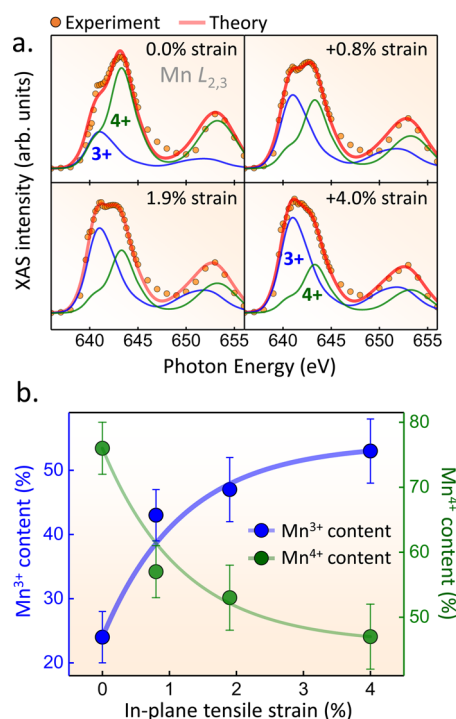


**Figure 2.** (a) Self-consistent simultaneous holistic fits of the strain-dependent experimental Mn  $L_{2,3}$  edge spectra using the  $\text{Mn}^{3+}$  and  $\text{Mn}^{4+}$  spectral components obtained via atomic multiplet theoretical calculations.<sup>46</sup> Resultant  $\text{Mn}^{3+}$  and  $\text{Mn}^{4+}$  ionic contents are plotted as a function of in-plane tensile strain in (b) and exhibit strain dependence similar to those of the experimental features shown in Figure 1b.

species acting on all four data sets. Figure 2b shows the resultant compositions and their corresponding uncertainties. Other relevant parameters obtained from the fitting are tabulated in Table S1 of the Supporting Information.

Similar measurements and spectroscopic analysis carried out for the identical set of  $\text{CaMnO}_3$  films grown during the same run but without the protective Pt capping layer suggests that the vacancies partially diffuse out of the film when exposed to ambient atmosphere (see Figure S1 in the Supporting Information). The uncapped films are still subjected to the same systematically varying substrate-induced coherent tensile strain as the capped samples; however, the spectral shapes for the strained films on  $\text{LaSrAlO}_4$  and  $\text{LaAlO}_3$  substrates (0.8% and 1.9% strain, respectively) look virtually indistinguishable from that for the bulk-like  $\text{CaMnO}_3$  film with predominantly  $\text{Mn}^{4+}$  valence (black spectrum). Significant spectral shape changes, fully consistent with the increase in the  $\text{Mn}^{3+}$  ion concentration as described above, are only observed for the maximally strained film on the LSAT substrate (green spectrum), but to a lesser extent when compared to the similar capped sample (see Figure 1a). Our observations confirm the prediction that equilibrium room-temperature oxygen vacancy concentrations are low and that oxygen vacancies remain mobile even at low temperatures and can diffuse out of the film when exposed to ambient atmosphere.<sup>15</sup> We emphasize that, while strain strongly enhances the oxygen vacancy concentration (by about an order of magnitude at 650 K and a factor of 5 at 950 K, the enhancement actually being stronger at low temperature), the small absolute oxygen vacancy concentration at room temperature makes the change in  $\text{Mn}^{3+}$  concentration undetectable by XAS. Using the Pt capping layer, we block

oxygen uptake by the film and preserve the increased high-temperature oxygen vacancy concentration that is metastable at room temperature. This furthermore underlines the importance of nondestructive bulk-sensitive X-ray techniques, such as XAS and HAXPES, capable of probing electronic properties of films that are buried underneath protective capping layers.

Figure 3 shows bulk-sensitive HAXPES measurements of the Mn 3s multiplet-split spectra for the Pt-capped coherently

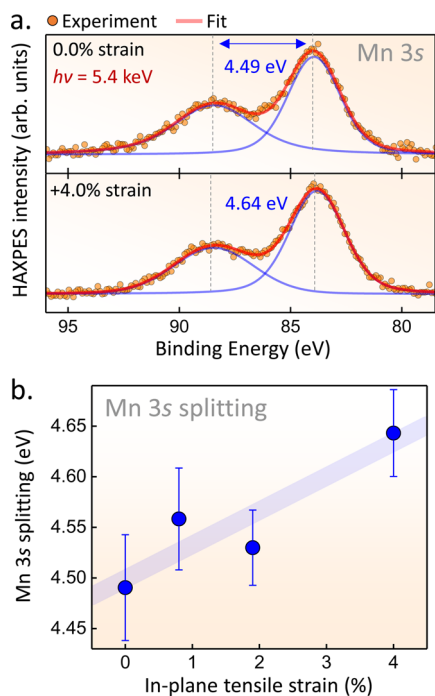


**Figure 3.** (a) Bulk-sensitive HAXPES of the Mn valence state in the  $\text{CaMnO}_3$  buried layers. Mn 3s core-level spectra measured with the photon energy of 5.4 keV exhibit well-understood splitting due to the exchange coupling interaction.<sup>38</sup> Magnitude of the splitting, quantified using self-consistent peak-fitting and shown for the fully relaxed (0% strain) and fully strained (+4% strain) films, can be related to the mean valence state of the Mn ions in the film.<sup>40</sup> (b) Magnitude of the Mn 3s peak splitting in the strained  $\text{CaMnO}_3$  films plotted as a function of in-plane tensile strain exhibits a trend that suggests systematic increase in the  $\text{Mn}^{3+}$  ion content, consistent with the result obtained via XAS spectroscopy as well as the calculations of oxygen vacancy formation energies.

strained  $\text{CaMnO}_3$  films. In 3d transition metals, the 3s core-level splitting arises due to the exchange coupling interaction between the 3s core-hole and 3d electrons and due to the intrashell 3d charge transfer process.<sup>37,38</sup> As the valence state of the Mn ion tends to decrease, the energy splitting between the two Mn 3s multiplet components increases.<sup>38,39</sup> Therefore, the 3s splitting is highly sensitive to the changes in the valence state of Mn ions and, in fact, has been used in numerous prior studies to determine the Mn valence state.<sup>39</sup> Self-consistent Shirley-background subtraction and peak-fitting reveals that the Mn 3s splitting increases systematically with in-plane tensile strain (see Figure 3b). The low value of 4.49 eV is observed for the fully relaxed bulk-like film (see Figure 3a), consistent with the prior studies and indicating predominantly  $\text{Mn}^{4+}$  ion content.<sup>40–42</sup> The high value of 4.64 eV is observed for the maximally strained (+4.0% tensile) film on the LSAT substrate (see Figure 3a), indicating a significant contribution of the lower-valent  $\text{Mn}^{3+}$  ions, consistent with the XAS results. By

assuming a homogeneous linear combination of the  $\text{Mn}^{3+}$  and  $\text{Mn}^{4+}$  concentrations in the film, as a first-order approximation we estimate that the maximally strained  $\text{CaMnO}_3$  film on the LSAT substrate contains up to 20% more  $\text{Mn}^{3+}$  ions compared to the fully relaxed film, which is in excellent agreement with the results of the holistic fitting of the XAS spectra (see Figure 2b).

Lastly, we utilized the combination of high-resolution XAS at the O K absorption edge and first-principle density-of-states calculations to probe the electronic defect states in the conduction band of  $\text{CaMnO}_3$ . The O K edge XAS probes the O 2p-projected unoccupied density of states resulting from dipole-allowed X-ray transitions from the 1s core-shell.<sup>43,44</sup> It is well-known that the few-eV-wide region immediately above the absorption threshold (pre-edge) provides access to the relevant states in the unoccupied  $\text{CaMnO}_3$  conduction band via O 2p–Mn 3d orbital hybridization.<sup>43,44</sup> Therefore, since these 2p–3d hybridized states are highly sensitive to the oxygen octahedral distortions as well as to the presence of oxygen vacancies, O K pre-edge XAS can be effectively used to detect electronic states induced by such defects<sup>45</sup> and to analyze electronic-structural changes resulting in vacancy formation.<sup>45</sup> While ground-state density-of-states calculations do not allow us to directly predict spectral shapes, we can tie the existence of spectral features to predicted changes in the energies of states.

In Figure 4a we plot the O K pre-edge XAS spectra for the same set of coherently strained Pt-capped  $\text{CaMnO}_3$  films. The

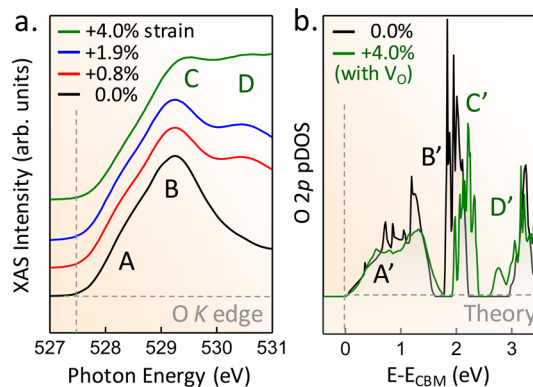


**Figure 4.** (a) XAS spectra of the O K pre-edge region shown for systematically varying in-plane tensile strain exhibit a line shape evolution consistent with first-principles predicted changes in O 2p projected density-of-states shown in (b) (only one of the equivalent antiferromagnetic spin channels is shown). Peak positions and shifts calculated for the fully relaxed and fully strained films are in good agreement with the experimental data, with correspondences seen between features A–D in experiment and A'–D' in theory. States A' correspond to hybridized majority-spin Mn  $e_g$ –O 2p states, while B' and C' are hybridized minority-spin Mn  $t_{2g}$ –O 2p states that are shifted to higher energy with increasing strain. The defect state D' results from lowering of hybridized minority-spin Mn  $e_g$ –O 2p states adjacent to the vacancy.

most significant strain-dependent modification of the line shape is observed as a feature (D) on the higher-energy side of the pre-edge peak (centered at 530.5 eV) growing systematically with increasing strain. Based on first-principles calculations (see Supporting Information for details) of the O 2p-projected density of states (pDOS) shown for the highest (+4.0%, with oxygen vacancy) and lowest (0.0%, without oxygen vacancy) strain states in Figure 4b, we can assign this feature to the

emerging defect state (D'). Similarly to the defect state in the band gap about 0.5 eV below the conduction-band edge,<sup>15</sup> which results from a lowering in energy of hybridized majority-spin Mn  $e_g$ -O 2p states adjacent to a formed vacancy, this state (D') results from an energy lowering of the minority-spin Mn  $e_g$ -O 2p states. Moreover, we can associate the observed shift of the peak (C) at 4% strain with an upward shift of the hybridized minority-spin Mn  $t_{2g}$ -O 2p states with increasing strain (C').

In summary, we experimentally varied the oxygen vacancy defect formation energies in strongly correlated oxide CaMnO<sub>3</sub> by engineering ultrathin coherently strained single-crystalline films via atomic layer-by-layer PLD from two separate targets. Oxygen vacancy content was stabilized by protecting the surfaces of the films with thin Pt layers in situ. By utilizing bulk-sensitive X-ray techniques, such as high-resolution XAS and HAXPES, as well as first-principles theory, we probed the electronic-structural changes related to the defect formation in CaMnO<sub>3</sub> and established a direct link between the coherent in-plane strain and the oxygen-vacancy content. Our results provide a new recipe for designing strongly correlated transition-metal oxides with tunable ionic defect content.

## ■ ASSOCIATED CONTENT

### Supporting Information

The Supporting Information is available free of charge on the ACS Publications website at DOI: [10.1021/acs.nanolett.6b03986](https://doi.org/10.1021/acs.nanolett.6b03986).

Sample synthesis and characterization, calculations, XAS of uncapped CaMnO<sub>3</sub> films, and parameters obtained for multiplet simulations (PDF)

## ■ AUTHOR INFORMATION

### Corresponding Author

\*E-mail: [axgray@temple.edu](mailto:axgray@temple.edu).

### ORCID

Ravini U. Chandrasena: [0000-0001-8766-0965](https://orcid.org/0000-0001-8766-0965)

Ulrich Aschauer: [0000-0002-1165-6377](https://orcid.org/0000-0002-1165-6377)

### Notes

The authors declare no competing financial interest.

## ■ ACKNOWLEDGMENTS

A.X.G., R.U.C., and W.Y. acknowledge support from the U.S. Army Research Office, under Grant No. W911NF-15-1-0181. The sample preparation by atomic layer-by-layer PLD was supported by the U.S. Department of Energy, Office of Science, under Grant No. DE-SC0004764 (Q.Y.L. and X.X.X.). Part of this work was financially supported by the ETH Zürich and by the ERC Advanced Grant program, No. 291151. Computer resources were provided by the ETH Zürich (Euler cluster) and the Swiss Supercomputing Center (CSCS) under project s624. M.U.D.J. and F.M.F.d.G. are thankful to the European research Council (ERC) for their support under advanced grant XRAYonACTIVE (No. 340279). The Advanced Light Source is supported by the Director, Office of Science, Office of Basic Energy Sciences, US Department of Energy under Contract No. DE-AC02-05CH11231.

## ■ REFERENCES

- (1) Kalinin, S. V.; Spaldin, N. A. *Science* **2013**, *341*, 858–859.
- (2) Jeong, J.; Aetukuri, N.; Graf, T.; Schladt, T. D.; Samant, M. G.; Parkin, S. S. P. *Science* **2013**, *339*, 1402–1405.

- (3) Veal, B. W.; Kim, S. K.; Zapol, P.; Iddir, H.; Baldo, P. M.; Eastman, J. A. *Nat. Commun.* **2016**, *7*, 11892.

- (4) Rodríguez Torres, C. E.; Pasquevich, G. A.; Zélis, P. M.; Golmar, F.; Heluani, S. P.; Nayak, S. K.; Adeagbo, W. A.; Hergert, W.; Hoffmann, M.; Ernst, A.; Esquinazi, P.; Stewart, S. J. *Phys. Rev. B: Condens. Matter Mater. Phys.* **2014**, *89*, 104411.

- (5) Aetukuri, N. B.; Gray, A. X.; Drouard, M.; Cossale, M.; Gao, L.; Reid, A. H.; Kukreja, R.; Ohldag, H.; Jenkins, C. A.; Arenholz, E.; Roche, K. P.; Durr, H. A.; Samant, M. G.; Parkin, S. S. P. *Nat. Phys.* **2013**, *9*, 661–666.

- (6) Locquet, J. P.; Perret, J.; Fompeyrine, J.; Machler, E.; Seo, J. W.; Van Tendeloo, G. *Nature* **1998**, *394*, 453–456.

- (7) Choi, K. J.; Biegalski, M.; Li, Y. L.; Sharan, A.; Schubert, J.; Uecker, R.; Reiche, P.; Chen, Y. B.; Pan, X. Q.; Gopalan, V.; Chen, L.-Q.; Schlom, D. G.; Eom, C. B. *Science* **2004**, *306*, 1005–1009.

- (8) Haeni, J. H.; Irvin, P.; Chang, W.; Uecker, R.; Reiche, P.; Li, Y. L.; Choudhury, S.; Tian, W.; Hawley, M. E.; Craigo, B.; Tagantsev, A. K.; Pan, X. Q.; Streiffner, S. K.; Chen, L. Q.; Kirchoefer, S. W.; Levy, J.; Schlom, D. G. *Nature* **2004**, *430*, 758–761.

- (9) Pertsev, N. A.; Tagantsev, A. K.; Setter, N. *Phys. Rev. B: Condens. Matter Mater. Phys.* **2000**, *61*, R825–R829.

- (10) Takahashi, K. S.; Kawasaki, M.; Tokura, Y. *Appl. Phys. Lett.* **2001**, *79*, 1324–1326.

- (11) Bhattacharjee, S.; Bousquet, E.; Ghosez, P. *Phys. Rev. Lett.* **2009**, *102*, 117602.

- (12) Hongwei, W.; Lixin, H.; Xifan, W. *EPL (Europhysics Letters)* **2012**, *100*, 17005.

- (13) Yamada, H.; Marinova, M.; Altuntas, P.; Crassous, A.; Bégon-Lours, L.; Fusil, S.; Jacquet, E.; Garcia, V.; Bouzehouane, K.; Gloter, A.; Villegas, J. E.; Barthélémy, A.; Bibes, M. *Sci. Rep.* **2013**, *3*, 2834.

- (14) Grutter, A. J.; Kirby, B. J.; Gray, M. T.; Flint, C. L.; Alaan, U. S.; Suzuki, Y.; Borchers, J. A. *Phys. Rev. Lett.* **2015**, *115*, 047601.

- (15) Aschauer, U.; Pfenninger, R.; Selbach, S. M.; Grande, T.; Spaldin, N. A. *Phys. Rev. B: Condens. Matter Mater. Phys.* **2013**, *88*, 054111.

- (16) Becher, C.; Maurel, L.; Aschauer, U.; Lilienblum, M.; Magén, C.; Meier, D.; Langenberg, E.; Trassin, M.; Blasco, J.; Krug, I. P.; Algarabel, P. A.; Spaldin, N. A.; Pardo, J. A.; Fiebig, M. *Nat. Nanotechnol.* **2015**, *10*, 661–665.

- (17) Kubicek, M.; Cai, Z.; Ma, W.; Yildiz, B.; Hutter, H.; Fleig, J. *ACS Nano* **2013**, *7*, 3276–3286.

- (18) Petrie, J. R.; Mitra, C.; Jeon, H.; Choi, W. S.; Meyer, T. L.; Reboredo, F. A.; Freeland, J. W.; Eres, G.; Lee, H. N. *Adv. Funct. Mater.* **2016**, *26*, 1564–1570.

- (19) Lei, Q.; Golalikhani, M.; Davidson, B. A.; Liu, G.; Schlom, D. G.; Qiao, Q.; Zhu, Y.; Chandrasena, R. U.; Yang, W.; Gray, A. X.; Arenholz, E.; Farrar, A. K.; Tenne, D. A.; Hu, M.; Guo, J.; Singh, R. K.; Xi, X. X. arXiv preprint:1610.06885, 2016.

- (20) Imbrenda, D.; Yang, D.; Wang, H.; Akbashev, A. R.; Kasaei, L.; Davidson, B. A.; Wu, X.; Xi, X.; Spanier, J. E. *Appl. Phys. Lett.* **2016**, *108*, 082902.

- (21) Young, A. T.; Arenholz, E.; Feng, J.; Padmore, H.; Marks, S.; Schlueter, R.; Hoyer, E.; Kelez, N.; Steier, C. *Surf. Rev. Lett.* **2002**, *09*, 549–554.

- (22) Kobayashi, K.; Kobata, M.; Iwai, H. *J. Electron Spectrosc. Relat. Phenom.* **2013**, *190*, 210–221.

- (23) Tanuma, S.; Powell, C. J.; Penn, D. R. *Surf. Interface Anal.* **2011**, *43*, 689–713.

- (24) Zeng, Z.; Greenblatt, M.; Croft, M. *Phys. Rev. B: Condens. Matter Mater. Phys.* **1999**, *59*, 8784–8788.

- (25) Cramer, S. P.; DeGroot, F. M. F.; Ma, Y.; Chen, C. T.; Sette, F.; Kipke, C. A.; Eichhorn, D. M.; Chan, M. K.; Armstrong, W. H. *J. Am. Chem. Soc.* **1991**, *113*, 7937–7940.

- (26) Qiao, R.; Chin, T.; Harris, S. J.; Yan, S.; Yang, W. *Curr. Appl. Phys.* **2013**, *13*, 544–548.

- (27) Abbate, M.; de Groot, F. M. F.; Fuggle, J. C.; Fujimori, A.; Strebel, O.; Lopez, F.; Domke, M.; Kaindl, G.; Sawatzky, G. A.; Takano, M.; Takeda, Y.; Eisaki, H.; Uchida, S. *Phys. Rev. B: Condens. Matter Mater. Phys.* **1992**, *46*, 4511–4519.

- (28) de Groot, F. M. F. *J. Electron Spectrosc. Relat. Phenom.* **1994**, *67*, 529–622.
- (29) Mierwaldt, D.; Mildner, S.; Arrigo, R.; Knop-Gericke, A.; Franke, E.; Blumenstein, A.; Hoffmann, J.; Jooss, C. *Catalysts* **2014**, *4*, 129.
- (30) Belli, M.; Scafati, A.; Bianconi, A.; Mobilio, S.; Palladino, L.; Reale, A.; Burattini, E. *Solid State Commun.* **1980**, *35*, 355–361.
- (31) Aruta, C.; Balestrino, G.; Tebano, A.; Ghiringhelli, G.; Brookes, N. B. *Europhys. Lett.* **2007**, *80*, 37003.
- (32) Toulemonde, O.; Studer, F.; Llobet, A.; Ranno, L.; Maignan, A.; Pollert, E.; Nevriya, M.; Pellegrin, E.; Brooks, N. B.; Goedkoop, J. J. *Magn. Magn. Mater.* **1998**, *190*, 307–317.
- (33) Varela, M.; Oxley, M. P.; Luo, W.; Tao, J.; Watanabe, M.; Lupini, A. R.; Pantelides, S. T.; Pennycook, S. J. *Phys. Rev. B: Condens. Matter Mater. Phys.* **2009**, *79*, 085117.
- (34) Kurata, H.; Colliex, C. *Phys. Rev. B: Condens. Matter Mater. Phys.* **1993**, *48*, 2102–2108.
- (35) Delgado-Jaime, M. U.; Kennepohl, P. *J. Synchrotron Radiat.* **2010**, *17*, 119–128.
- (36) Delgado-Jaime, M. U.; Mewis, C. P.; Kennepohl, P. *J. Synchrotron Radiat.* **2010**, *17*, 132–137.
- (37) Fadley, C. S.; Shirley, D. A. *Phys. Rev. A: At., Mol., Opt. Phys.* **1970**, *2*, 1109–1120.
- (38) Galakhov, V. R.; Demeter, M.; Bartkowski, S.; Neumann, M.; Ovechkina, N. A.; Kurmaev, E. Z.; Lobachevskaya, N. I.; Mukovskii, Y. M.; Mitchell, J.; Ederer, D. L. *Phys. Rev. B: Condens. Matter Mater. Phys.* **2002**, *65*, 113102.
- (39) Beyreuther, E.; Grafström, S.; Eng, L. M.; Thiele, C.; Dörr, K. *Phys. Rev. B: Condens. Matter Mater. Phys.* **2006**, *73*, 155425.
- (40) Ning, X.; Wang, Z.; Zhang, Z. *Sci. Rep.* **2015**, *5*, 8460.
- (41) Ning, X. K.; Wang, Z. J.; Chen, Y. N.; Zhang, Z. D. *Nanoscale* **2015**, *7*, 20635–20641.
- (42) Wu, Q.-H.; Liu, M.; Jaegermann, W. *Mater. Lett.* **2005**, *59*, 1980–1983.
- (43) de Groot, F. M. F.; Grioni, M.; Fuggle, J. C.; Ghijsen, J.; Sawatzky, G. A.; Petersen, H. *Phys. Rev. B: Condens. Matter Mater. Phys.* **1989**, *40*, 5715–5723.
- (44) Suntivich, J.; Hong, W. T.; Lee, Y.-L.; Rondinelli, J. M.; Yang, W.; Goodenough, J. B.; Dabrowski, B.; Freeland, J. W.; Shao-Horn, Y. *J. Phys. Chem. C* **2014**, *118*, 1856–1863.
- (45) Abbate, M.; Zampieri, G.; Prado, F.; Caneiro, A.; Gonzalez-Calbet, J. M.; Vallet-Regi, M. *Phys. Rev. B: Condens. Matter Mater. Phys.* **2002**, *65*, 155101.
- (46) Ghiasi, M.; Delgado-Jaime, M. U.; Malekzadeh, A.; Wang, R.-P.; Miedema, P. S.; Beye, M.; de Groot, F. M. F. *J. Phys. Chem. C* **2016**, *120*, 8167–8174.